

EPIC 220501947 b and K2-237 b: two transiting hot Jupiters

A. M. S. Smith,^{1*} Sz. Csizmadia¹, D. Gandolfi², S. Albrecht³, R. Alonso^{4,5}, O. Barragán², J. Cabrera¹, W. D. Cochran⁶, F. Dai⁷, H. Deeg^{4,5}, Ph. Eigmüller^{1,8}, M. Endl⁶, A. Erikson¹, M. Fridlund^{9,10,4}, A. Fukui^{11,4}, S. Grziwa¹², E. W. Guenther¹³, A. P. Hatzes¹³, D. Hidalgo^{4,5}, T. Hirano¹⁴, J. Korth¹², M. Kuzuhara^{15,16}, J. Livingston¹⁷, N. Narita^{17,15,16,4}, D. Nespral^{4,5}, P. Niraula¹⁸, G. Nowak^{4,5}, E. Pallé^{4,5}, M. Pätzold¹², C.M. Persson¹⁰, J. Prieto-Arranz^{4,5}, H. Rauer^{1,8,19}, S. Redfield¹⁸, I. Ribas^{20,21}, and V. Van Eylen⁹

¹*Institute of Planetary Research, German Aerospace Center, Rutherfordstrasse 2, 12489 Berlin, Germany*

²*Dipartimento di Fisica, Università di Torino, Via P. Giuria 1, I-10125, Torino, Italy*

³*Stellar Astrophysics Centre, Department of Physics and Astronomy, Aarhus University, Ny Munkegade 120, DK-8000 Aarhus C, Denmark*

⁴*Instituto de Astrofísica de Canarias (IAC), 38205 La Laguna, Tenerife, Spain*

⁵*Departamento de Astrofísica, Universidad de La Laguna (ULL), 38206 La Laguna, Tenerife, Spain*

⁶*Department of Astronomy and McDonald Observatory, University of Texas at Austin, 2515 Speedway, Stop C1400, Austin, TX 78712, USA*

⁷*Department of Physics and Kavli Institute for Astrophysics and Space Research, Massachusetts Institute of Technology, Cambridge, MA 02139, USA*

⁸*Center for Astronomy and Astrophysics, TU Berlin, Hardenbergstr. 36, 10623 Berlin, Germany*

⁹*Leiden Observatory, Leiden University, 2333CA Leiden, The Netherlands*

¹⁰*Chalmers University of Technology, Department of Space, Earth and Environment, Onsala Space Observatory, SE-439 92 Onsala, Sweden.*

¹¹*Subaru Telescope Okayama Branch Office, National Astronomical Observatory of Japan, NINS, 3037-5 Honjo, Kamogata, Asakuchi, Okayama 719-0232, Japan*

¹²*Rheinisches Institut für Umweltforschung an der Universität zu Köln, Aachener Strasse 209, 50931 Köln, Germany*

¹³*Thüringer Landessternwarte Tautenburg, Sternwarte 5, 07778 Tautenburg, Germany*

¹⁴*Department of Earth and Planetary Sciences, Tokyo Institute of Technology, 2-12-1 Ookayama, Meguro-ku, Tokyo 152-8551, Japan*

¹⁵*Astrobiology Center, NINS, 2-21-1 Osawa, Mitaka, Tokyo 181-8588, Japan*

¹⁶*National Astronomical Observatory of Japan, NINS, 2-21-1 Osawa, Mitaka, Tokyo 181-8588, Japan*

¹⁷*Department of Astronomy, The University of Tokyo, 7-3-1 Hongo, Bunkyo-ku, Tokyo 113-0033, Japan*

¹⁸*Astronomy Department and Van Vleck Observatory, Wesleyan University, Middletown, CT 06459, USA*

¹⁹*Institute of Geological Sciences, Freie Universität Berlin, Malteserstr. 74-100, 12249 Berlin, Germany*

²⁰*Institut de Ciències de l'Espai (ICE, CSIC), Campus UAB, Can Magrans s/n, 08193 Bellaterra, Spain*

²¹*Institut d'Estudis Espacials de Catalunya (IEEC), 08034 Barcelona, Spain*

Accepted XXX. Received YYY; in original form 2018 July 16

ABSTRACT

We report the discovery from K2 of two transiting hot Jupiter systems. EPIC 220501947 (observed in Campaign 8) is a K5 dwarf which hosts a planet slightly smaller than Jupiter, orbiting with a period of 4.0 d. We have made an independent discovery of K2-237 b (Campaign 11), which orbits an F6 dwarf every 2.2 d and has an inflated radius 50 – 60 per cent larger than that of Jupiter. We use high-precision radial velocity measurements, obtained using the HARPS and FIES spectrographs, to measure the planetary masses. We find that EPIC 220501947 b has a similar mass to Saturn, while K2-237 b is a little more massive than Jupiter.

Key words: planetary systems – planets and satellites: detection – planets and satellites: individual: EPIC 220501947 – planets and satellites: individual: K2-237

1 INTRODUCTION

Two decades after the discovery of the first hot Jupiter, there remains much to be understood about these intrinsically rare objects (e.g. [Howard et al. 2012](#)). Open questions concern the formation and migration of hot Jupiters, as well as the nature of the mechanism responsible for their inflation.

Most well-characterised hot Jupiter systems were discovered by wide-field, ground-based surveys such as WASP ([Pollacco et al. 2006](#)) and HAT ([Bakos et al. 2002](#)). Recently, the *K2* mission ([Howell et al. 2014](#)) has been used to discover such systems, and can determine planetary radii to greater precision. Ground-based radial velocity (RV) observations remain crucial, not only to confirm the planetary nature of the system, but to enable a fuller characterisation by measuring the planet-to-star mass ratio. It is only by increasing the sample of hot Jupiter systems with well-measured properties that we will be able to more fully understand them.

In particular, hot Jupiters, particularly low-density or inflated planets, are attractive targets for atmospheric characterisation (e.g. [Seager & Deming 2010](#); [Sing et al. 2016](#)). In addition, detections of evaporating atmospheres often come from this same sample (Lyman-alpha: [Vidal-Madjar et al. 2003](#); H-alpha: [Jensen et al. 2012](#); HeI: [Spake et al. 2018](#)) and represent a possible mechanism for the transformation of hot gas giants into hot rocky super-Earths ([Valencia et al. 2010](#); [Lopez et al. 2012](#)).

In this paper we report the discovery, under the auspices of the KESPRINT collaboration¹, of EPIC 220501947 and K2-237, two transiting hot Jupiter systems observed in K2 Campaigns 8 and 11, respectively. We use radial velocity follow-up measurements to confirm the planetary nature of the systems, and to measure the planetary masses. The discovery of K2-237 was recently reported by [Soto et al. \(2018\)](#), who measured the planet’s mass using RVs from the CORALIE and HARPS instruments. Here, we report an independent discovery of the same planetary system, and confirm their conclusion that the planet is inflated. We also perform a joint analysis incorporating the radial velocity data obtained by [Soto et al. \(2018\)](#).

2 OBSERVATIONS

2.1 *K2* photometry

EPIC 220501947 was observed as part of *K2*’s Campaign 8, from 2016 January 04 to 2016 March 23. K2-237 was observed as part of Campaign 11, which ran from 2016 September 24 to 2016 December 07. A change in the roll attitude of the spacecraft was required part way through the observing campaign. This has the effect that the C11 data are divided into two segments, with a 76-hour gap between 2016 October 18 and 21 where no observations were made².

We used two different detection codes to search the publicly available light curves, produced by the authors of [Vanderburg & Johnson \(2014\)](#), for periodic transit-like signals. EXOTRANS / VARLET ([Grziwa et al. 2012](#); [Grziwa & Pätzold](#)

Table 1. Catalogue information for EPIC 220501947 and K2-237.

Parameter	EPIC 220501947	K2-237
RA (J2000.0)	01h18m26.376s	16h55m04.534s
Dec (J2000.0)	+06° 49′ 00.74″	−28° 42′ 38.03″
pmRA* (mas yr ^{−1})	54.98 ± 0.05	−8.57 ± 0.10
pmDec* (mas yr ^{−1})	−34.96 ± 0.04	−5.56 ± 0.05
parallax* (mas)	4.27 ± 0.03	3.15 ± 0.07
Magnitudes		
<i>B</i>	15.07 ± 0.08	12.19 ± 0.07
<i>g</i> ′	14.55 ± 0.04	11.83 ± 0.06
<i>V</i>	13.95 ± 0.04	11.60 ± 0.05
<i>r</i> ′	13.46 ± 0.03	11.45 ± 0.03
<i>Kepler</i>	13.54	11.47
<i>i</i> ′	13.10 ± 0.06	11.31 ± 0.04
<i>J</i> (2MASS)	11.81 ± 0.03	10.51 ± 0.02
<i>H</i> (2MASS)	11.26 ± 0.02	10.27 ± 0.02
<i>K</i> (2MASS)	11.14 ± 0.03	10.22 ± 0.02
Additional identifiers:		
EPIC	220501947 (C8)	229426032 (C11)
UCAC	485-001859	307-097169
2MASS	01182635+0649004	16550453-2842380

*Data taken from Gaia DR2.

2016) and DST ([Cabrera et al. 2012](#)) detected consistent signals for both EPIC 220501947 and K2-237. EPIC 220501947 undergoes transits of about 2 per cent depth, approximately every 4 days, whereas the transits of K2-237 are around 1.5 per cent deep, and repeat every 2.2 days. This system was also detected using the BLS algorithm and an optimized frequency grid, described by [Ofir \(2014\)](#).

We also note that EPIC 220501947 was recently reported as a planetary candidate by [Petigura et al. \(2018\)](#), who report stellar properties for this target, determined from a Keck/HIRES spectrum using SPECMATCH-EMP ([Yee et al. 2017](#)). The values reported by [Petigura et al. \(2018\)](#) are in good agreement with those obtained from our independent data and analysis (see Section 3.2).

2.2 High resolution imaging

2.2.1 EPIC 220501947

We obtained high resolution/contrast images of EPIC 220501947 using the Infrared Camera and Spectrograph (IRCS; [Kobayashi et al. 2000](#)) on Subaru with the adaptive-optics system (AO188; [Hayano et al. 2010](#)) on UT 2016 November 7. We observed the target with the *H*-band filter and fine-sampling mode (1 pix = 0″.02057). For EPIC 220501947, both saturated (36 s) and unsaturated (4.5 s) frames were repeatedly obtained with the five-point dithering, which were used for the search for faint companions and absolute flux calibration, respectively. The total scientific exposure amounted to 540 s for the saturated frames.

2.2.2 K2-237

We observed K2-237 with the Multi-color Simultaneous Camera for studying Atmospheres of Transiting exoplanets (MuSCAT; [Narita et al. 2015](#)), mounted on the 1.88-

¹ <http://www.iac.es/proyecto/kesprint>

² See *K2* Data Release Notes at <https://keplerscience.arc.nasa.gov/k2-data-release-notes.html>

m telescope at the Okayama Astronomical Observatory. We conducted observations on UT 2017 August 7, obtaining 30 images with the exposure time of 2.5 s in the second generation Sloan g' , r' , and z' bands. The pixel scale of $0.36''/\text{pixel}$ and the median seeing of $2.1''$ allows the detection of faint objects a few arcseconds away from the target star.

We also performed Lucky Imaging (LI) of K2-237 using the FastCam camera (Oscoz et al. 2008) on the 1.55-meter Telescopio Carlos Sánchez (TCS) at Observatorio del Teide, Tenerife. FastCam is a very low noise and fast readout speed EMCCD camera with 512×512 pixels (with a physical pixel size of 16 microns, and a FoV of $21.2'' \times 21.2''$). During the night of 2017 July 19 (UT), 10,000 individual frames of K2-237 were collected in the Johnson-Cousins I-band (infrared), with an exposure time of 50 ms for each frame.

2.3 Spectroscopic observations

2.3.1 Tull

We obtained a single reconnaissance spectrum with the Robert G. Tull coude spectrograph (Tull et al. 1995) on the 2.7-m Harlan J. Smith Telescope at McDonald Observatory, Texas. The observation was conducted on 2016 October 13, and the exposure time was 1611 s, yielding $S/N = 35$ per resolution element at 565 nm.

2.3.2 FIES

Radial velocity (RV) observations were performed using the Fibre-fed Échelle Spectrograph (FIES; Frandsen & Lindberg 1999; Telting et al. 2014) mounted at the 2.56-m Nordic Optical Telescope (NOT) of Roque de los Muchachos Observatory (La Palma, Spain). We employed the *med-res* fibre for EPIC 220501947 and the *high-res* fibre for K2-237, resulting in resolving powers, $R = \lambda/\Delta\lambda \approx 47\,000$ and $67\,000$, respectively. We took three consecutive exposures of 900-1200 sec per observation epoch to remove cosmic ray hits. We traced the intra-exposure RV drift of the instrument by acquiring long-exposed (~ 40 sec) ThAr spectra immediately before and after the target observations (Gandolfi et al. 2015). The data was reduced using standard IRAF and IDL routines, which include bias subtraction, flat fielding, order tracing and extraction, and wavelength calibration. The RV measurements of EPIC 220501947 and K2-237 were extracted via multi-order cross-correlations with a FIES spectrum of the RV standard stars HD 190007 and HD 168009, respectively. Seven measurements of EPIC 220501947 were secured between October 2006 and January 2017 under the observing programs 54-027 and 54-205. Eight FIES spectra of K2-237 were gathered between July and August 2017 as part of the observing programs 55-019 and OPTICON 17A/064.

2.3.3 HARPS

Additionally, we acquired seven high-resolution spectra ($R \approx 115\,000$) with the HARPS spectrograph (Mayor et al. 2003) based on the ESO 3.6-m telescope at La Silla Observatory (Chile). The observations were performed between in August 2017 as part of the ESO programme 099.C-0491. We set the exposure time to 900–1800 seconds and used the second fibre to monitor the sky background. We reduced

Table 2. Radial velocity measurements.

BJD _{TDB} −2450000	RV km s ^{−1}	σ_{RV} km s ^{−1}	BIS km s ^{−1}	Inst. [†]
EPIC 220501947				
7668.668055	−16.569	0.017	0.028	F
7669.555227	−16.657	0.012	0.035	F
7682.549665	−16.656	0.018	0.052	F
7684.536591	−16.576	0.019	0.034	F
7717.374193	−16.610	0.012	0.040	F
7769.395395	−16.612	0.020	0.025	F
7777.384377	−16.584	0.018	0.022	F
K2-237				
7954.463961	−22.354	0.027	0.022	F
7955.456791	−22.641	0.061	−0.086	F
7956.432724	−22.463	0.053	0.040	F
7964.393400	−22.707	0.067	0.086	F
7965.402076	−22.354	0.045	0.003	F
7966.393358	−22.625	0.042	−0.088	F
7980.391270	−22.496	0.068	0.012	F
7981.389387	−22.562	0.050	−0.022	F
7984.556027	−22.362	0.011	−0.019	H
7985.483048	−22.213	0.016	−0.046	H
7986.559244	−22.433	0.022	0.056	H
7987.509317	−22.164	0.015	−0.038	H
7990.472080	−22.480	0.015	0.098	H
7991.487944	−22.208	0.012	−0.083	H
7992.484469	−22.426	0.009	−0.029	H

[†] F = FIES, H = HARPS

Table 3. Adopted stellar parameters. See Sections 3.2 and 3.3 for a full discussion of how these values were derived.

Parameter	EPIC 220501947	K2-237
$T_{*,\text{eff}}/\text{K}$	4444 ± 70	6099 ± 110
R_*/R_\odot	0.71 ± 0.04	1.34 ± 0.03
[Fe/H] (dex)	0.14 ± 0.12	0.00 ± 0.08
M_*/M_\odot	0.74 ± 0.04	1.22 ± 0.05
$v \sin i_*/\text{km s}^{-1}$	2.2 ± 0.3	12 ± 1
Distance / pc	234 ± 2	318 ± 7
Spectral type	K5 V	F6 V

the data with the on-line HARPS pipeline and extracted the RVs by cross-correlating the HARPS spectra with a G2 numerical mask (Baranne et al. 1996; Pepe et al. 2002).

All of our RV measurements are listed in Table 2 along with their 1σ uncertainties and the bisector spans of the cross-correlation functions.

3 STELLAR CHARACTERISATION

3.1 Method

We adopt the following procedure to derive masses and radii for our two host stars. In each case, we analyse a single co-added spectrum using SPECMATCH-EMP (Yee et al. 2017), to determine the stellar effective temperature, $T_{*,\text{eff}}$, the stellar

radius, R_* , and the stellar metallicity, $[\text{Fe}/\text{H}]$. SPECMATCH-EMP compares a stellar spectrum to spectra from a library of well-characterised stars. This stellar library contains 404 stars ranging from F1 to M5 in spectral type, which have high-resolution ($R \approx 60\,000$) Keck/HIRES spectra, as well as properties derived from other observations (interferometry, asteroseismology, spectrophotometry) and from LTE spectral synthesis.

The uncertainties on the radii from SPECMATCH-EMP are relatively large, particularly in the case of the hotter K2-237. We therefore instead choose to use the $T_{*,\text{eff}}$ and $[\text{Fe}/\text{H}]$ values from SPECMATCH-EMP, and the stellar density, ρ_* , determined from the transit light curves (Section 5), as inputs to the empirical relations of Southworth (2011). These relations are based on 90 detached eclipsing binary systems, and can be used to compute the stellar mass and radius. The masses and radii derived in this way are reported, along with the temperatures and metallicities from SPECMATCH-EMP, in Table 3.

3.2 EPIC 220501947

For EPIC 220501947, we used a co-added spectrum comprised of the seven FIES spectra. The stellar radius value from the SPECMATCH-EMP analysis is $0.72 \pm 0.07 R_\odot$, which is in excellent agreement with the value derived using Southworth’s empirical relations (Section 3.1, Table 3).

A spectral analysis was also performed on the Tull reconnaissance spectrum, using KEA (Endl & Cochran 2016), yielding parameters $T_{*,\text{eff}} = 4680 \pm 97$ K, $\log g_* = 4.38 \pm 0.16$ (cgs) (cf. 4.62 ± 0.04 for our adopted M_* , R_*), and $[\text{Fe}/\text{H}] = -0.24 \pm 0.10$, which are in reasonable agreement with those from SPECMATCH-EMP, and $v \sin i_* = 2.2 \pm 0.3 \text{ km s}^{-1}$.

Petigura et al. (2018) report stellar parameters for EPIC 220501947, based on a Keck/HIRES spectrum. We find that our values are in excellent agreement with theirs ($T_{*,\text{eff}} = 4398 \pm 70$ K, $[\text{Fe}/\text{H}] = 0.17 \pm 0.12$, and $R_* = 0.73 \pm 0.1 R_\odot$). Finally, we used the parallax value from the second data release of the Gaia mission (Gaia Collaboration et al. 2016, 2018), along with the bolometric correction ($BC_G = -0.236 \pm 0.013$ mag) of Andrae et al. (2018) and our $T_{*,\text{eff}}$ value to estimate the stellar radius of EPIC 220501947, assuming zero extinction. We derive a radius of $0.77 \pm 0.03 R_\odot$, which is in good agreement with our adopted value.

3.3 K2-237

The seven HARPS spectra of K2-237 were co-added, and analysed using the method described above. The radius derived using SPECMATCH-EMP is $1.36 \pm 0.22 R_\odot$, which agrees well with our adopted value (Table 3). As a check, we also analysed the same co-added spectrum using SME (Spectroscopy Made Easy; Valenti & Piskunov 1996; Valenti & Fischer 2005) with ATLAS 12 model spectra (Kurucz 2013) and pre-calculated atomic parameters from the VALD3 database (Ryabchikova et al. 2011, 2015). The microturbulent velocity was fixed to 1.3 km s^{-1} (Bruntt et al. 2010), and the macroturbulent velocity to 5.2 km s^{-1} (Doyle et al. 2014). The results of our SME analysis ($T_{*,\text{eff}} = 6220 \pm 120$ K, $[\text{Fe}/\text{H}] = 0.15 \pm 0.15$, $\log g_* = 4.28 \pm 0.12$) are also in excellent agreement with our adopted values ($\log g_* = 4.27 \pm 0.02$).

A further comparison was made to the stellar parameters available at the ‘ExoFOP-K2’ website³ which were generated using the methodology of Huber et al. (2016). These parameters have very much larger uncertainties than our parameters, but all parameters except stellar density agree to within 1σ . The stellar density reported on ExoFOP ($234 \pm 267 \text{ kg m}^{-3}$) is somewhat inconsistent with our value (1.8σ), and we also note that the mass and radius given on ExoFOP result in a higher density of around 420 kg m^{-3} . Using the Gaia DR2 parallax and extinction ($A_G = 0.25 \pm 0.18$ mag) values, and $BC_G = 0.076 \pm 0.034$ mag, we find $R_* = 1.39 \pm 0.13 R_\odot$, which is within 1σ of our adopted value.

We also compared our stellar parameters to those derived by Soto et al. (2018). The mass and radius estimates are in reasonably good agreement, with the values of Soto et al. (2018) around 1σ larger than ours. This is probably explained by the higher temperature found by Soto et al. (2018) ($T_{*,\text{eff}} = 6257 \pm 100$ K); using this temperature and our stellar density as inputs to the Southworth (2011) relations, we get a stellar radius very close to their value. We note, however, that the stellar density implied by the Soto et al. (2018) mass and radius values ($\rho_* = 0.44 \pm 0.06$) is inconsistent at more than 5σ with their quoted density value ($\rho_* = 0.102^{+0.012}_{-0.010}$). In solar units, our derived stellar density (from light curve modelling) is $\rho_* = 0.50 \pm 0.03 \rho_\odot$. It is unclear how the density quoted by Soto et al. (2018) was derived.

3.3.1 Stellar rotation

We computed a Lomb-Scargle periodogram using the light curve further decorrelated using a polynomial fit, and with in-transit points removed. We found a peak at around 5.1 d, which we attribute to stellar rotation. The amplitude of this rotational variability varies over the course of the K2 observations, and was strongest in the first part of the light curve.

This detected period closely matches that found by Soto et al. (2018) (5.07 ± 0.02 d). Using their period and our stellar radius and $v \sin i_*$ (from SME) values, we determine the stellar inclination angle, $i_* = 64^{+14}_{-9}$ degrees. This is larger than the $51.56^{+3.73}_{-2.80}$ degrees determined by Soto et al. (2018), and we also note that our 2σ error bar encompasses 90° . We would therefore caution against concluding that the stellar spin and planetary orbital axes are misaligned; our smaller stellar radius is consistent with them being aligned or near-aligned.

3.4 Distances

The distances quoted in Table 3 are derived from the parallaxes listed in the second GAIA data release (Gaia Collaboration et al. 2016, 2018). They are in good agreement with distances calculated from estimates of the absolute magnitude, albeit with significantly smaller uncertainties. In particular, we note that the Gaia distance to K2-237 is consis-

³ https://exofop.ipac.caltech.edu/k2/edit_target.php?id=229426032

tent with that derived by Soto et al. (2018), but that the Gaia uncertainty is approximately 20 times smaller.

3.5 Ages

3.5.1 EPIC 220501947

We plotted EPIC 220501947 alongside isochrones of various ages, following the approach of e.g. Smith et al. (2014), but using the Dartmouth isochrones (Dotter et al. 2008). The age is poorly-constrained - the 1σ uncertainties span all ages greater than about 8.5 Gyr. We note, however, that these uncertainties are probably underestimated, since we do not account for the uncertainty on the metallicity, nor the systematic errors in the Dartmouth stellar models.

3.5.2 K2-237

Plotting K2-237 alongside theoretical isochrones (Dotter et al. 2008) yields a best-fitting age of approximately 6 ± 1 Gyr. Using the 5.1-d rotation period (Section 3.3.1) and $B - V$ colour (Table 1) as inputs to the gyrochronology relations derived by Barnes (2007), we derive an age of $0.3^{+0.2}_{-0.1}$ Gyr (2σ uncertainties: $0.3^{+1.6}_{-0.1}$ Gyr). We note, however, that ages derived from isochrones and from gyrochronology often disagree for planet-host stars (Brown 2014; Maxted et al. 2015), perhaps because hot Jupiters tidally interact with their host stars, spinning them up.

4 CONTAMINATION FROM NEIGHBOURING OBJECTS

4.1 EPIC 220501947

The Subaru/IRCS data were reduced following the procedure in Hirano et al. (2016), and we obtained the calibrated combined images for the saturated and unsaturated frames respectively. To estimate the achieved contrast of the saturated image, we computed the flux scatter within the annulus as a function of angular separation from the centroid of the star. Fig. 1 plots the 5σ contrast curve together with the target image with the field-of-view of $4'' \times 4''$. EPIC 220501947 is a single star to the detection limit, meaning that the light curve is free from contamination from nearby objects.

4.2 K2-237

The MuSCAT imaging reveals K2-237 to be in a rather crowded field, with several faint objects nearby. Using the r' band image (Fig. 2), we detected a total of ten objects fainter than the target within the photometric aperture used to generate the light curve. The total flux contribution of these objects relative to the target flux is 0.042. We adopt this value for the quantity of contaminating ‘third’ light, and conservatively estimate an uncertainty of half, i.e. 0.021 – to account for measurement errors and the difference between the Kepler and r' bandpasses. This has the effect of changing the planet radius at approximately the 1σ level.

We constructed a high-resolution image by co-adding

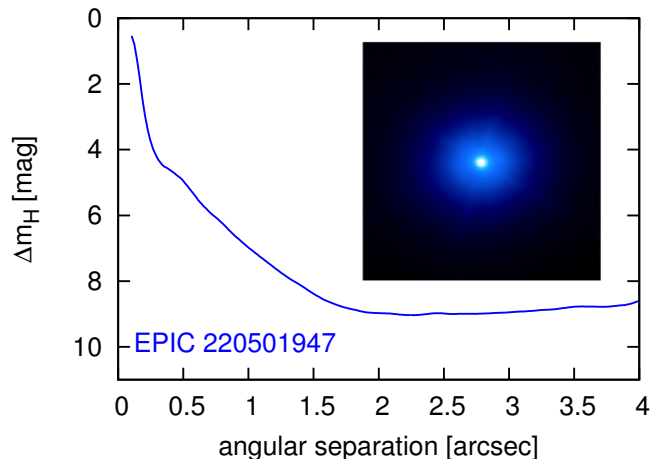


Figure 1. Results of Subaru IRCS imaging of EPIC 220501947. The curve indicates the 5σ detection limit, as a function of angular separation, and the inset image ($4'' \times 4''$, North is up, East is left) indicates that there is no evidence for any close companions to EPIC 220501947.

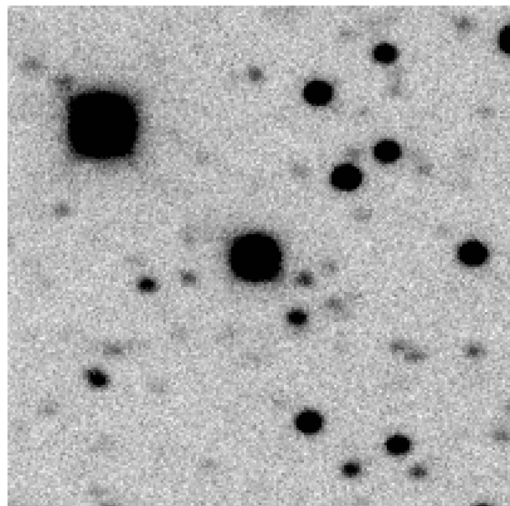


Figure 2. MuSCAT r -band image, centred on K2-237. North is up, East is to the left, and the image is $72'' \times 72''$. A number of faint contaminating stars can be seen in the close vicinity of the target.

the best thirty per cent of the TCS/FastCam images, giving a total exposure time of 150 s. The typical Strehl ratio of these images is about 0.07. In order to construct the co-added image, each individual frame was bias-subtracted, aligned and co-added and then processed with the FastCam dedicated software developed at the Universidad Polit cnica de Cartagena (Labadie et al. 2010; J dar et al. 2013). Fig. 3 shows the contrast curve that was computed based on the scatter within the annulus as a function of angular separation from the target centroid.

Three neighbouring objects were found in the image, at separations from K2-237 of between $7''$ and $11''$. The relative fluxes of these objects are consistent with those determined

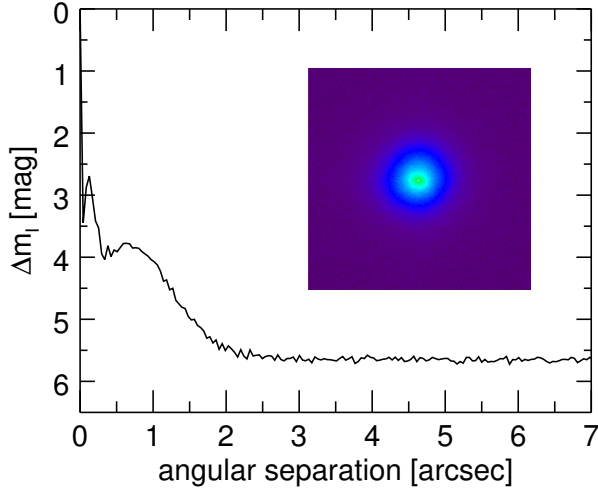


Figure 3. I-band magnitude contrast curve as a function of angular separation up to $7.0''$ from K2-237 obtained with the FastCam camera at TCS. The solid line indicates the 5σ detection limit for the primary star. The inset shows the $7'' \times 7''$ combined image of K2-237. North is up and East is left.

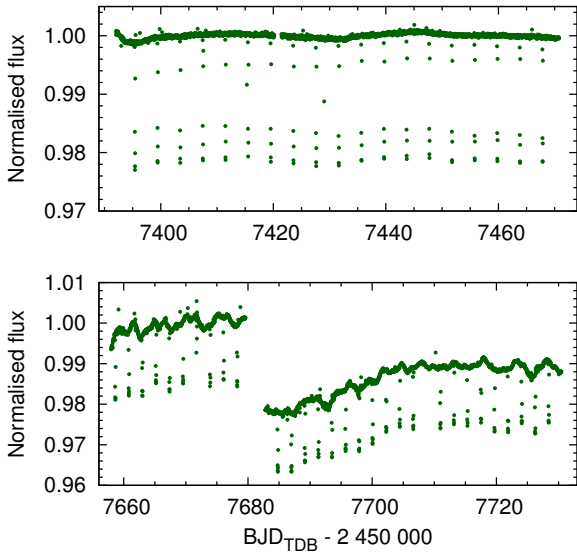


Figure 4. *K2* light curves for EPIC 220501947 (upper panel) and K2-237 (lower panel). The EPIC 220501947 light curve was produced using the EVEREST code (Luger et al. 2016), and the K2-237 light curve by Andrew Vanderburg (following Vanderburg & Johnson 2014). The discontinuity in the lower panel is a result of a change in the roll angle of *K2* during Campaign 11 (see Section 2.1 for further details).

by MuSCAT. No bright companions were detected within $7''$ of the target (Fig. 3).

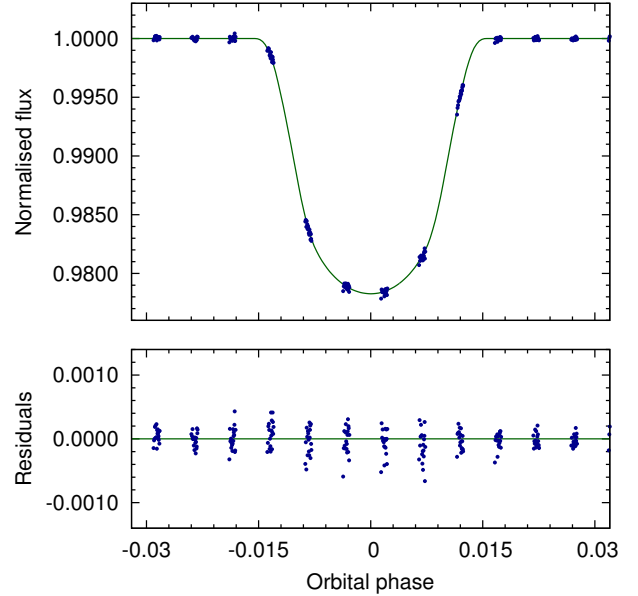


Figure 5. Phase-folded *K2* photometry (blue circles) and best-fitting model (solid green line) for EPIC 220501947, with residuals to the model shown in the lower panel. The light curve is that of Luger et al. (2016).

5 DETERMINATION OF SYSTEM PARAMETERS

5.1 Light curve preparation

5.1.1 EPIC 220501947

We use the EVEREST (Luger et al. 2016) *K2* light curve for EPIC 220501947 (Fig. 4, upper panel). For modelling the transit (Section 5), we cut the light curve into pieces, selecting only those light curve points within two transit durations of the transit midtime for modelling. This results in a series of light curve sections of length $4T_{14}$ (approximately 10 hours in the case of EPIC 220501947), centred on the midpoint of each transit. Each section of the light curve is detrended using a quadratic function of time to remove the remaining signatures of stellar variability. Finally, we remove three obvious outliers from the light curve.

5.1.2 K2-237

For K2-237, we perform the same procedure as above, but we instead use the light curve of Vanderburg & Johnson (2014) (lower panel of Fig. 4). In addition to the transits, the light curve exhibits a quasi-periodic signal which we attribute to stellar rotational variability and investigate further in Section 3.3.1.

5.2 The TLCM code

We model each system using the TRANSIT AND LIGHT CURVE MODELLER (TLCM) code. TLCM has been used to model exoplanet light curves and radial velocities in numerous previous studies, including planets discovered in long-cadence *K2* data (e.g. K2-99b; Smith et al. 2017). The code

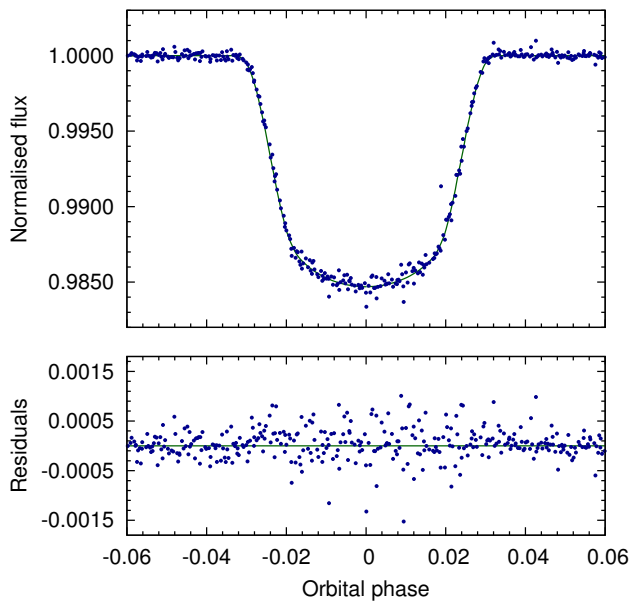


Figure 6. Phase-folded *K2* photometry (blue circles) and best-fitting model (solid green line) for K2-237, with residuals to the model shown in the lower panel. The light curve is that of Vanderburg & Johnson (2014).

is described in Csizmadia et al. (2015), and a more detailed description will accompany the first public release of the code (Csizmadia, under review).

In brief, TLCM fits the photometric transit using the Mandel & Agol (2002) model, compensating for *K2*'s long exposure times using numerical integration, and simultaneously fits a Keplerian orbit to the RV data. TLCM uses the combination of a genetic algorithm to find the approximate global minimum, followed by simulated annealing and Markov-chain Monte Carlo phases to refine the solution, and explore the neighbouring parameter space for the determination of uncertainties on the model parameters.

5.3 Combined fit

For our basic fit, we fit for the following parameters: the orbital period, P , the epoch of mid-transit, T_0 , the scaled semi-major axis (a/R_*), planet-to-stellar radius ratio (R_p/R_*), the impact parameter, b , the limb-darkening parameters, u_+ and u_- (see below), the systemic stellar RV, γ , and the RV semi-amplitude, K . In the case of K2-237, for which we have RV data from FIES and HARPS, we also fit the systematic offset between these two instruments, γ_{F-H} .

5.4 Limb darkening

Limb-darkening is parametrized using a quadratic model, whose coefficients, u_a and u_b are transformed to the fit parameters $u_+ = u_a + u_b$ and $u_- = u_a - u_b$. In the case of K2-237, u_+ and u_- are free parameters. For EPIC 220501947, the observational cadence of *K2* is close to an integer fraction of the orbital period. This results in clumps of data points in phase space, rather than the data being evenly distributed

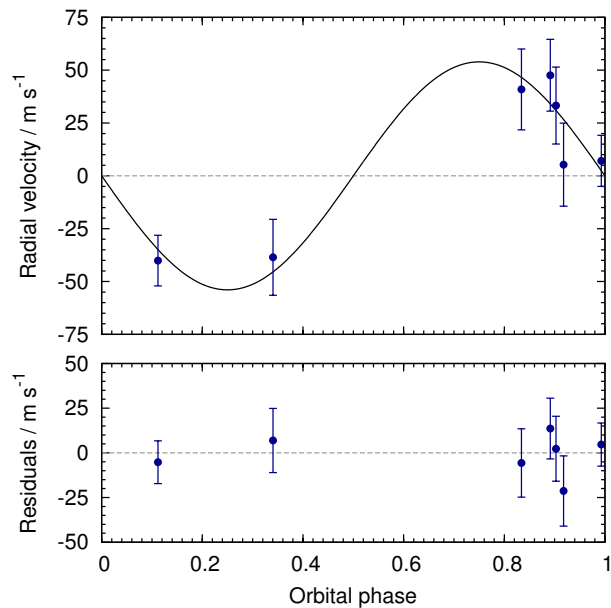


Figure 7. Radial velocities from FIES for EPIC 220501947. Our best-fitting model is shown with a solid black line, and the residuals to the model are plotted in the lower panel. The data are phase-folded, and the systemic radial velocity, γ , has been subtracted.

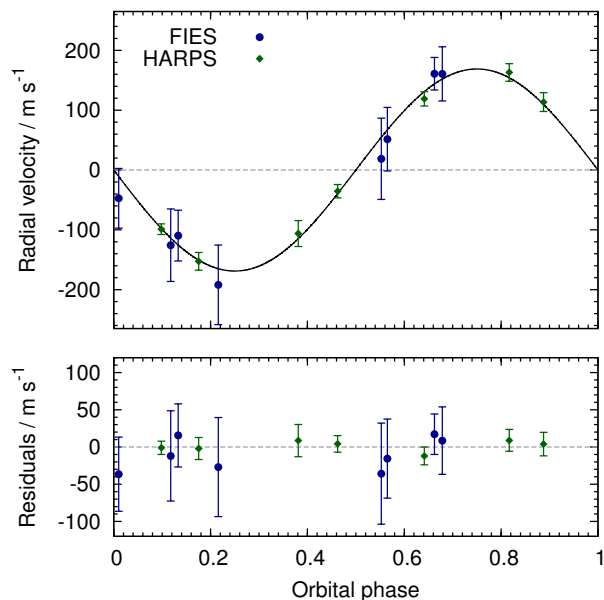


Figure 8. Radial velocities from FIES (blue circles) and HARPS (green squares) for K2-237. Our best-fitting model is shown with a solid black line, and the residuals to the model are plotted in the lower panel. The data are phase-folded, and the systemic radial velocity, γ , has been subtracted.

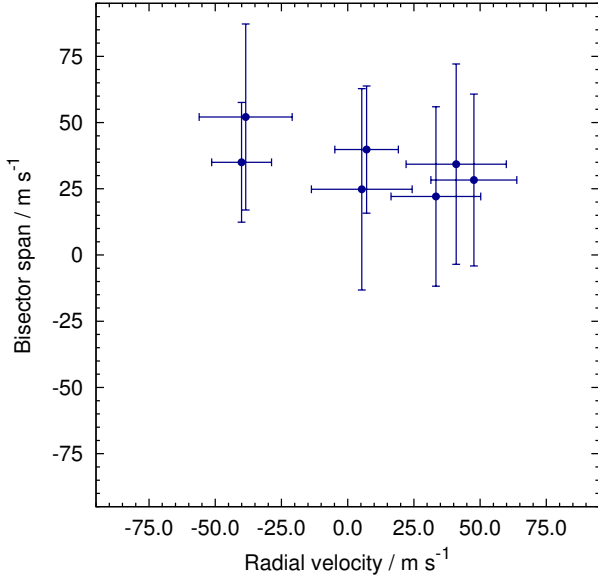


Figure 9. Bisector span as a function of radial velocity for EPIC 220501947. As in Fig. 7, the systemic radial velocity, γ , has been subtracted. The uncertainties in the bisector spans are taken to be twice those of the radial velocities.

in phase (Fig. 5). Transit ingress and egress are poorly covered, providing a weaker constraint on the limb-darkening parameters than would otherwise be the case. We therefore opt to constrain the limb-darkening parameters to take values close to (± 0.01) the theoretical values of Sing (2010) for the relevant stellar parameters and the *Kepler* bandpass ($u_+ = 0.7349$, $u_- = 0.5689$). We discuss this issue and related problems arising from the poor coverage of ingress and egress in Appendix A.

5.5 Orbital eccentricity

In our basic fit, we fix the orbital eccentricity to zero, but we also used TLCDM to fit for the orbital eccentricity, e , rather than forcing a circular orbital solution. The additional parameters we fit for in this case are $e \cos \omega$ and $e \sin \omega$, where ω is the argument of periastron. We used the χ^2 values of the resulting fits to calculate the Bayesian Information Criterion (BIC) in order to establish whether the improved RV fit justifies the additional model parameters.

For both systems, we found a larger BIC value for the eccentric fit (for EPIC 220501947 $\text{BIC}_{\text{ecc}} - \text{BIC}_{e=0} = 3.6$, and for K2-237, $\text{BIC}_{\text{ecc}} - \text{BIC}_{e=0} = 5.0$). For the purposes of calculating the BIC, we considered the number of data points to be the number of RV points only, since these provide most of the information regarding orbital eccentricity. Including the photometric data points in the total would increase the BIC values, making a circular orbit even more favourable. We note that for neither system is the best-fitting eccentricity found to be significant at the 3σ level, although the eccentricity of EPIC 220501947 is poorly-constrained because of the incomplete phase coverage of the RV data. We therefore adopt $e = 0$ for both systems, as expected given both theoretical predictions for close-in exoplanetary systems, and

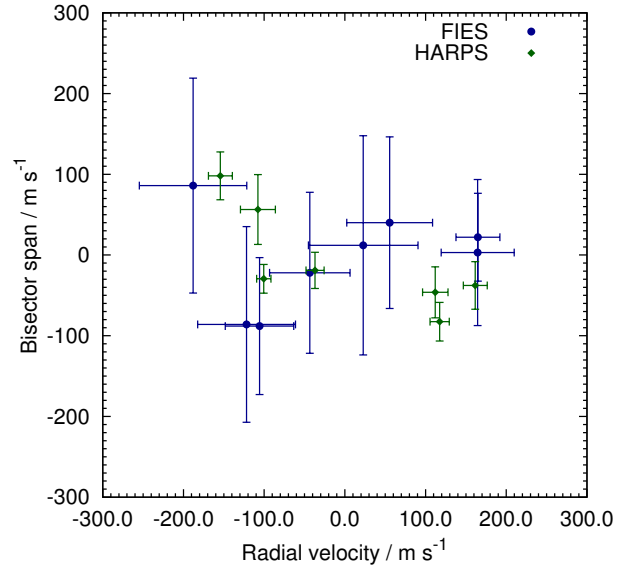


Figure 10. Bisector span as a function of radial velocity for K2-237. As in Fig. 8, the systemic radial velocity, γ , has been subtracted, as has the fitted RV offset between the FIES and HARPS instruments, $\gamma_{\text{F-H}}$. The uncertainties in the bisector spans are taken to be twice those of the radial velocities.

empirical evidence that such planets only rarely exist on significantly eccentric orbits (e.g. Anderson et al. 2012).

5.6 RV drift

We also tried fitting for a linear trend in the radial velocities of each star, the presence of which can be indicative of the presence of a third body in the system. In both cases, we found that the best-fitting radial acceleration is not significant, and that the BIC clearly favours the simpler model. In summary, there is no evidence for the presence of a third body in either system.

5.7 RV bisectors

A blended eclipsing binary can mimic a transiting planetary system, but will exhibit a correlation between the RV and the RV bisector spans (Queloz et al. 2001). In Figs. 9 and 10, we plot these two quantities, and find that there is no such correlation in either case, as expected for true planetary systems.

5.8 Additional photometric signals

We tried fitting for an occultation (centred on phase 0.5, given the evidence for circular orbits in both systems). No evidence was found for the presence of an occultation signal in the light curve of either system. Similarly, we found no compelling evidence of any transit timing variations (TTV) in either system. Interestingly, there seems to be a variation in the transit depth of K2-237 b. This explains the higher in-transit residual scatter observed in Fig. 6, which we suggest

is caused by stellar spots, which are also responsible for the rotational modulation seen in the light curve (Section 3.3.1).

5.9 Additional RV data

The RV semi-amplitude and planet mass that we determine for K2-237 differ somewhat from the values ($K = 210 \pm 10 \text{ ms}^{-1}$; $M_p = 1.60 \pm 0.11 M_{\text{Jup}}$) reported by Soto et al. (2018). We tried including their RVs (four measurements from HARPS, and nine from CORALIE) in our fit, and found that we require an offset between our HARPS measurements and theirs. We suggest that the need for this arises from the different reduction pipelines used to obtain the RVs from the HARPS spectra. Including the RVs of Soto et al. (2018) yields $K = 180_{-7}^{+3} \text{ ms}^{-1}$, which is compatible (at the $\approx 1\sigma$ level) with the value obtained from our data alone ($K = 169 \pm 5 \text{ ms}^{-1}$; Table 4), but almost 3σ from the value of Soto et al. (2018). The source of this apparent discrepancy is unclear.

5.10 Summary of system parameters

In summary, we find that the planet orbiting the K5 dwarf EPIC 220501947 in an approximately 4-d orbit is slightly larger and more massive than Saturn ($1.12 \pm 0.01 R_{\text{Sat}}$ and $1.12 \pm 0.04 M_{\text{Sat}}$). The planetary parameters reported in the planet candidate list of Petigura et al. (2018) (transit duration, impact parameter, and planetary radius) are in good agreement with those derived in our analysis.

K2-237 b, however, is typical of an inflated hot Jupiter – slightly more massive than Jupiter, but with a radius some 50 to 60 per cent larger than the largest planet in the Solar System. The planet orbits an F8 dwarf star.

6 DISCUSSION

Because we find a smaller stellar radius for K2-237 than do Soto et al. (2018), we also determine the planetary radius to be smaller. However, we still find the planet to be inflated, and with an incident flux of $2.5 \pm 0.2 \text{ MWm}^{-2}$, the planet is more inflated than predicted by Sestovic et al. (2018) (i.e. it still lies in the green region of Soto et al. (2018)'s Fig. 12).

The radius of EPIC 220501947 b seems to be fairly typical for a hot Saturn, slightly smaller than the similar HATS-6 b and WASP-83 b (Hartman et al. 2015; Hellier et al. 2015), but significantly larger than that of the anomalously dense HD 149026 b (Sato et al. 2005), which is thought to be extremely metal-rich (Spiegel et al. 2014).

ACKNOWLEDGEMENTS

This paper includes data collected by the Kepler mission. Funding for the Kepler mission is provided by the NASA Science Mission directorate. Some of the data presented in this paper were obtained from the Mikulski Archive for Space Telescopes (MAST). STScI is operated by the Association of Universities for Research in Astronomy, Inc., under NASA contract NAS5-26555. Support for MAST for non-HST data

is provided by the NASA Office of Space Science via grant NNX09AF08G and by other grants and contracts.

This research has made use of the Exoplanet Follow-up Observation Program website, which is operated by the California Institute of Technology, under contract with the National Aeronautics and Space Administration under the Exoplanet Exploration Program.

We greatly thank the NOT staff members for their precious support during the observations. Based on observations obtained with the Nordic Optical Telescope (NOT), operated on the island of La Palma jointly by Denmark, Finland, Iceland, Norway, and Sweden, in the Spanish Observatorio del Roque de los Muchachos (ORM) of the Instituto de Astrofísica de Canarias (IAC).

This research has made use of NASA's Astrophysics Data System, the SIMBAD data base, operated at CDS, Strasbourg, France, the Exoplanet Orbit Database and the Exoplanet Data Explorer at exoplanets.org, and the Exoplanets Encyclopaedia at exoplanet.eu. We also used Astropy, a community-developed core Python package for Astronomy (Astropy Collaboration et al. 2013).

This work has made use of data from the European Space Agency (ESA) mission *Gaia* (<https://www.cosmos.esa.int/gaia>), processed by the *Gaia* Data Processing and Analysis Consortium (DPAC, <https://www.cosmos.esa.int/web/gaia/dpac/consortium>). Funding for the DPAC has been provided by national institutions, in particular the institutions participating in the *Gaia* Multilateral Agreement.

D.G. gratefully acknowledges the financial support of the *Programma Giovani Ricercatori – Rita Levi Montalcini – Rientro dei Cervelli* (2012) awarded by the Italian Ministry of Education, Universities and Research (MIUR). Sz.Cs. thanks the Hungarian OTKA Grant K113117. M.E. and W.D.C. were supported by NASA grant NNX16AJ11G to The University of Texas at Austin. I.R. acknowledges support from the Spanish Ministry of Economy and Competitiveness (MINECO) and the Fondo Europeo de Desarrollo Regional (FEDER) through grant ESP2016-80435-C2-1-R, as well as the support of the Generalitat de Catalunya/CERCA programme. T.H. was supported by JSPS KAKENHI Grant Number JP16K17660. M.F. and C.M.P. gratefully acknowledge the support of the Swedish National Space Board. This work is partly supported by JSPS KAKENHI Grant Number JP18H01265.

Table 4. System parameters from TLMC modelling

Parameter	Symbol	Unit	EPIC 220501947	K2-237
<i>TLMC fitted parameters:</i>				
Orbital period	P	d	4.024866 ± 0.000014	2.1805567 ± 0.0000050
Epoch of mid-transit	T_0	BJD _{TDB}	$2457395.4140458 \pm 0.0000019$	$2457656.4633784 \pm 0.0000052$
Scaled orbital major semi-axis	a/R_*	—	$13.72^{+0.21}_{-0.51}$	$5.631^{+0.003}_{-0.187}$
Ratio of planetary to stellar radii	R_p/R_*	—	$0.1306^{+0.0017}_{-0.0007}$	$0.1173^{+0.0016}_{-0.0007}$
Transit impact parameter	b	—	0.18 ± 0.13	$0.451^{+0.066}_{-0.007}$
Limb-darkening parameters	u_+	—	$0.734 \pm 0.007^*$	$0.78^{+0.08}_{-0.06}$
	u_-	—	$0.569 \pm 0.007^*$	$-0.26^{+0.09}_{-0.24}$
Stellar orbital velocity semi-amplitude	K	m s ⁻¹	53.9 ± 2.0	$168.6^{+4.6}_{-3.1}$
Systemic radial velocity	γ	km s ⁻¹	-16.6171 ± 0.0012	$-22.5188^{+0.0083}_{-0.0078}$
Velocity offset between FIES and HARPS	γ_{F-H}	m s ⁻¹	—	$193.4^{+7.0}_{-9.7}$
<i>Derived parameters:</i>				
Orbital eccentricity (adopted)	e	...	0	0
Stellar density	ρ_*	kg m ⁻³	3018^{+143}_{-326}	711 ± 36
Planet mass	M_p	M _{Jup}	0.336 ± 0.012	1.231 ± 0.043
Planet radius	R_p	R _{Jup}	$0.947^{+0.012}_{-0.005}$	1.570 ± 0.054
Planet density	ρ_p	kg m ⁻³	522 ± 25	422 ± 46
Orbital major semi-axis	a	AU	$0.0467^{+0.0007}_{-0.0017}$	0.0352 ± 0.0010
Orbital inclination angle	i_p	°	$89.24^{+0.52}_{-0.65}$	85.4 ± 0.4
Transit duration	T_{14}	d	$0.1042^{+0.0011}_{-0.0007}$	0.1260 ± 0.0030
Planet equilibrium temperature [†]	$T_{p,eq,A=0}$	K	850^{+16}_{-7}	1817 ± 36

*For EPIC 220501947, the limb-darkening coefficients are not freely fitted - see Section 5.4 for details.

†The equilibrium temperature is calculated assuming a planetary albedo of zero, and isotropic re-radiation.

REFERENCES

- Anderson D. R., et al., 2012, *MNRAS*, **422**, 1988
- Andrae R., et al. 2018, *A&A*
- Astropy Collaboration et al., 2013, *A&A*, **558**, A33
- Bakos G. Á., Lázár J., Papp I., Sári P., Green E. M., 2002, *PASP*, **114**, 974
- Baranne A., et al., 1996, *A&AS*, **119**, 373
- Barnes S. A., 2007, *ApJ*, **669**, 1167
- Brown D. J. A., 2014, *MNRAS*, **442**, 1844
- Bruntt H., et al., 2010, *MNRAS*, **405**, 1907
- Cabrera J., Csizmadia S., Erikson A., Rauer H., Kirste S., 2012, *A&A*, **548**, A44
- Csizmadia S., Pasternacki T., Dreyer C., Cabrera J., Erikson A., Rauer H., 2013, *A&A*, **549**, A9
- Csizmadia S., et al., 2015, *A&A*, **584**, A13
- Dotter A., Chaboyer B., Jevremović D., Kostov V., Baron E., Ferguson J. W., 2008, *ApJS*, **178**, 89
- Doyle A. P., Davies G. R., Smalley B., Chaplin W. J., Elsworth Y., 2014, *MNRAS*, **444**, 3592
- Endl M., Cochran W. D., 2016, *PASP*, **128**, 094502
- Espinoza N., Jordán A., 2015, *MNRAS*, **450**, 1879
- Frandsen S., Lindberg B., 1999, in Karttunen H., Pirola V., eds, *Astrophysics with the NOT*. p. 71
- Gaia Collaboration et al., 2016, *A&A*, **595**, A1
- Gaia Collaboration et al., 2018, *A&A*
- Gandolfi D., et al., 2015, *A&A*, **576**, A11
- Grziwa S., Pätzold M., 2016, preprint, ([arXiv:1607.08417](https://arxiv.org/abs/1607.08417))
- Grziwa S., Pätzold M., Carone L., 2012, *MNRAS*, **420**, 1045
- Hartman J. D., et al., 2015, *AJ*, **149**, 166
- Hayano Y., et al., 2010, in *Adaptive Optics Systems II*. p. 77360N, [doi:10.1117/12.857567](https://doi.org/10.1117/12.857567)
- Hellier C., et al., 2015, *AJ*, **150**, 18
- Hirano T., et al., 2016, *ApJ*, **820**, 41
- Howard A. W., et al., 2012, *ApJS*, **201**, 15
- Howell S. B., et al., 2014, *PASP*, **126**, 398
- Huber D., et al., 2016, *ApJS*, **224**, 2
- Jensen A. G., Redfield S., Endl M., Cochran W. D., Koesterke L., Barman T., 2012, *ApJ*, **751**, 86
- Jódar E., Pérez-Garrido A., Díaz-Sánchez A., Villó I., Rebolo R., Pérez-Prieto J. A., 2013, *MNRAS*, **429**, 859
- Kobayashi N., et al., 2000, in Iye M., Moorwood A. F., eds, *Proc. SPIE Vol. 4008, Optical and IR Telescope Instrumentation and Detectors*. pp 1056–1066, [doi:10.1117/12.395423](https://doi.org/10.1117/12.395423)
- Kurucz R. L., 2013, *ATLAS12: Opacity sampling model atmosphere program*, Astrophysics Source Code Library ([ascl:1303.024](https://ui.adsabs.org/abs/2013ascl...1303024K))
- Labadie L., et al., 2010, in *Ground-based and Airborne Instrumentation for Astronomy III*. p. 77350X ([arXiv:1009.4710](https://arxiv.org/abs/1009.4710)), [doi:10.1117/12.857998](https://doi.org/10.1117/12.857998)
- Lopez E. D., Fortney J. J., Miller N., 2012, *ApJ*, **761**, 59
- Luger R., Agol E., Kruse E., Barnes R., Becker A., Foreman-Mackey D., Deming D., 2016, preprint, ([arXiv:1607.00524](https://arxiv.org/abs/1607.00524))
- Mandel K., Agol E., 2002, *ApJ*, **580**, L171
- Maxted P. F. L., Serenelli A. M., Southworth J., 2015, *A&A*, **577**, A90
- Mayor M., et al., 2003, *The Messenger*, **114**, 20
- Narita N., et al., 2015, *Journal of Astronomical Telescopes, Instruments, and Systems*, **1**, 045001
- Ofir A., 2014, *A&A*, **561**, A138
- Oscz A., et al., 2008, in *Ground-based and Airborne Instrumentation for Astronomy II*. p. 701447, [doi:10.1117/12.788834](https://doi.org/10.1117/12.788834)
- Pepe F., Mayor M., Galland F., Naef D., Queloz D., Santos N. C., Udry S., Burnet M., 2002, *A&A*, **388**, 632
- Petigura E. A., et al., 2018, *AJ*, **155**, 21
- Pollacco D. L., et al., 2006, *PASP*, **118**, 1407
- Queloz D., et al., 2001, *A&A*, **379**, 279
- Ryabchikova T. A., Pakhomov Y. V., Piskunov N. E., 2011, *Kazan Izdatel Kazanskogo Universiteta*, **153**, 61
- Ryabchikova T., Piskunov N., Kurucz R. L., Stempels H. C.,

- Heiter U., Pakhomov Y., Barklem P. S., 2015, *Phys. Scr.*, **90**, 054005
- Sato B., et al., 2005, *ApJ*, **633**, 465
- Seager S., Deming D., 2010, *ARA&A*, **48**, 631
- Sestovic M., Demory B.-O., Queloz D., 2018, preprint, ([arXiv:1804.03075](https://arxiv.org/abs/1804.03075))
- Sing D. K., 2010, *A&A*, **510**, A21
- Sing D. K., et al., 2016, *Nature*, **529**, 59
- Smith A. M. S., et al., 2014, *A&A*, **570**, A64
- Smith A. M. S., et al., 2017, *MNRAS*, **464**, 2708
- Soto M. G., et al., 2018, preprint, ([arXiv:1801.07959](https://arxiv.org/abs/1801.07959))
- Southworth J., 2011, *MNRAS*, **417**, 2166
- Spake J. J., et al., 2018, *Nature*, **557**, 68
- Spiegel D. S., Fortney J. J., Sotin C., 2014, *Proceedings of the National Academy of Science*, **111**, 12622
- Telting J. H., et al., 2014, *Astronomische Nachrichten*, **335**, 41
- Tull R. G., MacQueen P. J., Sneden C., Lambert D. L., 1995, *PASP*, **107**, 251
- Valencia D., Ikoma M., Guillot T., Nettelmann N., 2010, *A&A*, **516**, A20
- Valenti J. A., Fischer D. A., 2005, *ApJS*, **159**, 141
- Valenti J. A., Piskunov N., 1996, *A&AS*, **118**, 595
- Vanderburg A., Johnson J. A., 2014, *PASP*, **126**, 948
- Vidal-Madjar A., Lecavelier des Etangs A., Désert J.-M., Ballester G. E., Ferlet R., Hébrard G., Mayor M., 2003, *Nature*, **422**, 143
- Yee S. W., Petigura E. A., von Braun K., 2017, *ApJ*, **836**, 77

APPENDIX A: ISSUES ARISING FROM THE POORLY-SAMPLED LIGHT CURVE OF EPIC 220501947

As we mentioned in Section 5.4, and can be clearly seen in Fig. 5, the *K2* light curve of EPIC 220501947 is poorly-sampled in orbital phase. This is a result of the near-commensurability of the orbital period and the observational cadence. In this particular case, this leads to difficulty in determining the transit duration, and the physical parameters dependent on this.

The transit depth (and hence planet-to-star radius ratio) is well constrained by the data; there exists photometry close to the transit midpoint, and there is no problem in determining the out-of-transit baseline. However, there is no data covering any of the four contact points (the beginning and end of the ingress and egress phases). This results in little constraint on the duration of both the transit and of ingress and egress.

After fitting for the limb-darkening parameters as usual, we tried fixing them to the theoretical values of Sing (2010). We took the values corresponding to $\log g_* = 4.5$, $[\text{Fe}/\text{H}] = 0.1$, and $T_{*,\text{eff}} = 4500$ K. We allow these values to vary slightly (± 0.01), to account for the uncertainty in the stellar parameters, and for the fact that the coefficients are tabulated only for certain values of $\log g_*$, $[\text{Fe}/\text{H}]$, and $T_{*,\text{eff}}$. The allowed variation encompasses the limb-darkening parameters tabulated for neighbouring values of these parameters.

Our fits resulted in two families of solutions, revealing a degeneracy between a/R_* , b , and the limb-darkening coefficients. The two groups of solutions result in light curve fits which look nearly identical, but which have significantly different values of a/R_* , resulting in drastically different stellar densities. Instead of $a/R_* = 13.6$ and $b = 0.2$, the second solution has $a/R_* = 11.6$, $b = 0.3$, and limb-darkening co-

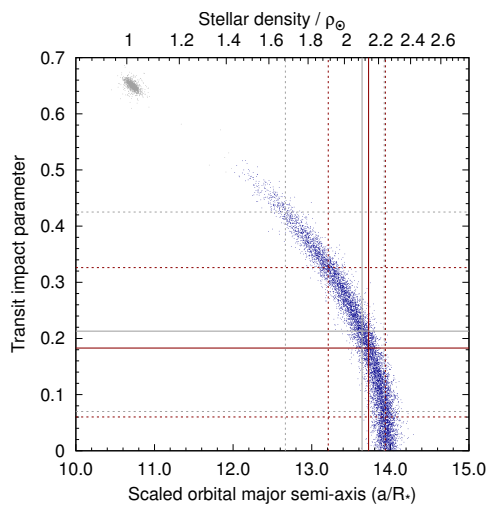


Figure A1. Posterior distribution of impact parameter and a/R_* , when the limb-darkening coefficients are constrained as described in the text. The corresponding stellar density is indicated along the top of the plot. A total of 10 000 randomly-selected samples from the posterior distribution are shown, with excluded points coloured grey. The red solid line indicates our adopted solution (median of remaining points), and the red dashed lines the 1σ confidence interval. The solid and dashed grey lines indicate the solution obtained without excluding the grey points in the top left.

efficients that lie far from any tabulated values ($u_+ = 1.7$, $u_- = -0.3$). The resulting stellar density (1800 kg m^{-3}) is inconsistent with our various stellar analyses (Section 3.2). Furthermore, adopting this less-dense value results in the star lying in a region of parameter space not covered by any of the Dartmouth isochrones (Dotter et al. 2008).

We find that even when constraining the limb-darkening coefficients, a small fraction of the MCMC posterior distribution lies in a distinct region of parameter space, with a stellar density far too low to be compatible with our knowledge of the star (Fig. A1). We therefore opt both to constrain the limb-darkening coefficients and to exclude solutions with $a/R_* < 12$ from the posterior distribution. This is illustrated in Fig. A1.

We note that previous studies have recommended fitting, rather than fixing limb-darkening coefficients, in order to avoid biasing the determination of the system parameters (Csizmadia et al. 2013; Espinoza & Jordán 2015). These studies did not consider poorly-sampled light curves such as that of EPIC 220501947, however. Fortunately, EPIC 220501947 lies in a region of parameter space where there is minimal difference between various tabulated limb-darkening coefficients; this is not true for all spectral types (Fig. 1 of Csizmadia et al. 2013).

This paper has been typeset from a $\text{T}_{\text{E}}\text{X}/\text{L}^{\text{A}}\text{T}_{\text{E}}\text{X}$ file prepared by the author.